

# Vibrational-Anharmonicity-Assisted Phase Transitions in Perovskite Oxides Under Terahertz Irradiation

Cong Zhou and Jian Zhou<sup>\*</sup>

*Center for Alloy Innovation and Design, State Key Laboratory for Mechanical Behavior of Materials, Xi'an Jiaotong University, Xi'an, 710049, China*



(Received 8 June 2023; accepted 18 July 2023; published 8 August 2023)

Despite extensive research interests in perovskite oxides, low-energy consumption, nondestructive, and manoeuverable methods for phase transition in perovskite oxides are still under exploration, and the underlying mechanisms remain ambiguous. Here, optical susceptibility, including electron and anharmonic phonon contributions, is used to evaluate Gibbs free-energy variations of  $\text{PbTiO}_3$  and  $\text{BaTiO}_3$  under terahertz irradiation. This corresponds to an off-resonant light-controlled phase transition, rather than the resonant approaches that excites hot carriers over electronic band or infrared-active vibrations in the phonon band. We show that intermediate terahertz light can trigger polarization change between ferroelectric orientation variants of  $\text{PbTiO}_3$  at room temperature. Similarly, the phase transformation from low-symmetric ferroelectric phase to high-symmetric paraelectric structure in  $\text{PbTiO}_3$  can be driven by changing the polarization and intensity of the incident light. Analogous results are obtained in  $\text{BaTiO}_3$ . In detail, the phonon spectrum and optical susceptibility exhibit strong temperature dependence, in which we show significant effects of anharmonic vibration. In order to explicitly show its nonlinear optical nature, we perform an alternating electric field dressed *ab initio* molecular dynamics simulation, which maps onto the Raman-active phonon excitation under off-resonant terahertz irradiation.

DOI: 10.1103/PhysRevApplied.20.024020

## I. INTRODUCTION

Since the discovery of ferroelectric (FE) materials over a century ago, they have possessed exotic applications, such as nonvolatile electronics with fast switching speed [1], light-electrical-mechanical energy conversion [2], nondestructive readout, capability of high-density integration, ultrafast data read and write kinetics [3], etc. Until now, the most widely studied ferroelectric material type is perovskite oxides, which exhibit polymorphic lattice structures under different environmental conditions, and could show ultrafast displacive phase transitions among them. Numerous studies have demonstrated that phase transition in perovskite oxides can be triggered via mechanical [4–6], thermal [7–9], and electrical approaches [10], while recent experimental advances have witnessed such phase transitions in titanates below band-gap light illumination [11,12]. Note that the atomic diffusionless motion in perovskites during collective phase transitions corresponds to the  $\Gamma$ -mode vibrations in the momentum space, in accordance with the long-wavelength feature of the optical field, which may largely reduce energy consumption and enhance its efficiency during phase transition. Theoretical computations have shown that electron excitation between

the valence and conduction bands could induce phase transformations in perovskite oxides, via strong coupling between phonon vibration and light-excited carriers [13]. In spite of these efforts, fundamental mechanisms of photoinduced structural change still await further exploration and understanding.

In this work, we use first-principles density-functional-theory (DFT) calculations, including anharmonic vibrational effects to show that controllable phase transitions in perovskite oxides could occur under off-resonant THz light irradiation. The THz optics has been considered as an advanced technique owing to its non-contacting, transparency, nondestructive, and athermic nature [14–17]. Hence, it holds great potential for various promising applications, including nondestructive check [18], food quality scan [19], security check [20], long-distance communication [21], and modern electronic devices [22,23]. We use two prototypical perovskite oxides, namely, lead titanate and barium titanate, to illustrate phase transitions under THz irradiation. The optical responses are evaluated through both electron and phonon contributions. We include anharmonic vibrational effects in the phonon dispersion, which could incorporate the thermal effects that have been largely ignored in conventional density-functional perturbation approaches. Through thermodynamic evaluations, we suggest two

\*jianzhou@xjtu.edu.cn

possible phase-transition paths under intermediate THz illumination. One is between two FE orientation variants (the Nambu-Goldstone mode in a Mexican-hat potential profile), and the other is between the low-symmetric FE phase and high-symmetric paraelectric (PE) structure (the Higgs mode). They would occur depending upon the THz polarization and intensity. Here, THz frequency is chosen to be away from the infrared (IR) active phonon mode at  $\Gamma$  in the first Brillouin zone (BZ). It corresponds to an off-resonant light-matter interaction, rather than generating electron-hole pairs or IR-active mode, ensuring its athermic nature. Hence, we predict an alternative approach from the previously discussed schemes [24–26] that an IR-active vibration generates the phase-transition responsible Raman modes, involving multiple (three or four) phonon scattering. We also perform an alternating electric field dressed *ab initio* molecular dynamics (AIMD) simulation to explicitly show that the Raman-active mode can be excited through this off-resonant light irradiation. This is consistent with the nonlinear optical process nature.

## II. METHODS

Our DFT calculations are performed in the Vienna *ab initio* simulation package (VASP) [27] that treats the exchange-correlation functional using the generalized gradient approximation (GGA) method in the solid-state Perdew-Burke-Ernzerhof (PBEsol) form [28]. Projector augmented-wave (PAW) method is used to treat the core electrons, yielding an accuracy compared with all-electron approaches [29,30]. The valence electrons (Ti:  $4s^23d^2$ , O:  $2s^22p^4$ , Pb:  $5d^{10}6s^26p^2$ , and Ba:  $5s^25p^66s^2$ ) are described by a plane-wave basis set with a kinetic cutoff energy of 500 and 550 eV for  $\text{PbTiO}_3$  and  $\text{BaTiO}_3$ , respectively. The first BZ is represented by Monkhorst-Pack  $k$ -mesh grids of  $(12 \times 12 \times 12)$  [31]. The total energy and force convergence criteria are set as  $1 \times 10^{-8}$  eV and  $1 \times 10^{-8}$  eV  $\text{\AA}^{-1}$ , respectively. The convergence of these computational parameters has been carefully tested. To include the anharmonic effect in the phonon dispersion, we adopt the self-consistent approach (SCPH scheme [32]) with microscopic anharmonic force constants extracted from density-functional calculations using the least absolute shrinkage and selection operator technique [33]. This method has been successful in reproducing the finite-temperature phonon dispersion of various polar solids, which exhibits well-consistent results with experimental observations. The simulation supercell is composed of  $(2 \times 2 \times 2)$  unit cells containing 40 atoms, which are used to generate force constants from randomly selected structures during AIMD simulations [34]. Nonanalytic correction is included by the Ewald method and the Born effective charge components are evaluated according to the density-functional perturbation

theory (DFPT). The Brillouin-zone sampling of vibrational free energy from the SCPH approach,  $F_{\text{vib}}^{(\text{SCPH})}(V, T)$ , is computed based on  $(20 \times 20 \times 20)$   $q$ -mesh grids in the first BZ. The trajectory of atomic motion under an alternating electric field is simulated by combining electric fields in the AIMD method. The temperature of 300 K and the microcanonical ensemble were selected as the simulation conditions. The zero-temperature equilibrium structure is used as the initial structure to ensure that no phonons are activated before simulation. DFPT calculation results are used as the reference basis for the projection of molecular dynamics trajectories into phonon modes.

## III. RESULTS

### A. Geometric, electronic, and phonon properties of $\text{PbTiO}_3$

We start our calculations with lead titanate ( $\text{PbTiO}_3$ ), which exhibits two typical phases [Figs. 1(a) and 1(b)]. The high-symmetric PE phase shows a cubic structure (space group of  $Pm\bar{3}m$ , no. 221), which usually appears under high temperature (above 766 K) in the conventional phase diagram. Our DFT calculations give its lattice parameters to be  $a = b = c = 3.92$  Å. Below the critical temperature,  $\text{PbTiO}_3$  undergoes an inversion symmetry breaking phase transition, resulting in a FE tetragonal structure (space group of  $P4mm$ , no. 99). The polar is parallel to the principal axes, namely,  $\langle 100 \rangle$  directions of the cubic phase (all together six equivalent directions). The lattice constant is slightly elongated along the polar direction (relaxed to be 4.09 Å), and the other two lattice parameters are equally to be 3.89 Å. These results agree well with the experimental measurements [35]. Note that the polarization direction could distinguish different FE phases with symmetrically equivalent states (e.g., orthogonal  $\text{FE}_1$  and  $\text{FE}_2$  orientational variants), separated by an energy barrier. Figure 1(c) schematically plots the potential energy surface as a function of electric polarization  $P_z$  and  $P_x$ . Due to the  $C_4$  rotation, there are four minima in the potential energy surface. The potential energy landscape of phase transitions between FE and PE is associated with longitudinal changes of polarization, similar to a Higgs mode [36]. The energy biasing between two different FE orientational variants ( $\text{FE}_1$  and  $\text{FE}_2$ ) corresponds to transverse changes of polarization, which belongs to a Nambu-Goldstone mode [36].

We plot the DFT-calculated electronic band dispersions of the FE and PE in Fig. 2(a). Here, we assume the electric polarization  $P$  in the FE phase along  $z$  ( $\text{FE}_1$ , nonzero  $P_z$ ). One sees that both phases are semiconductors with their band gaps being 1.45 (PE) and 1.42 eV (FE), consistent with their ionic compound nature. The valence-band maximum (VBM) of PE locates at the equivalent  $X$ ,  $Y$ , and  $Z$  points. In the FE phase, the valley band energy at  $Z$  reduces

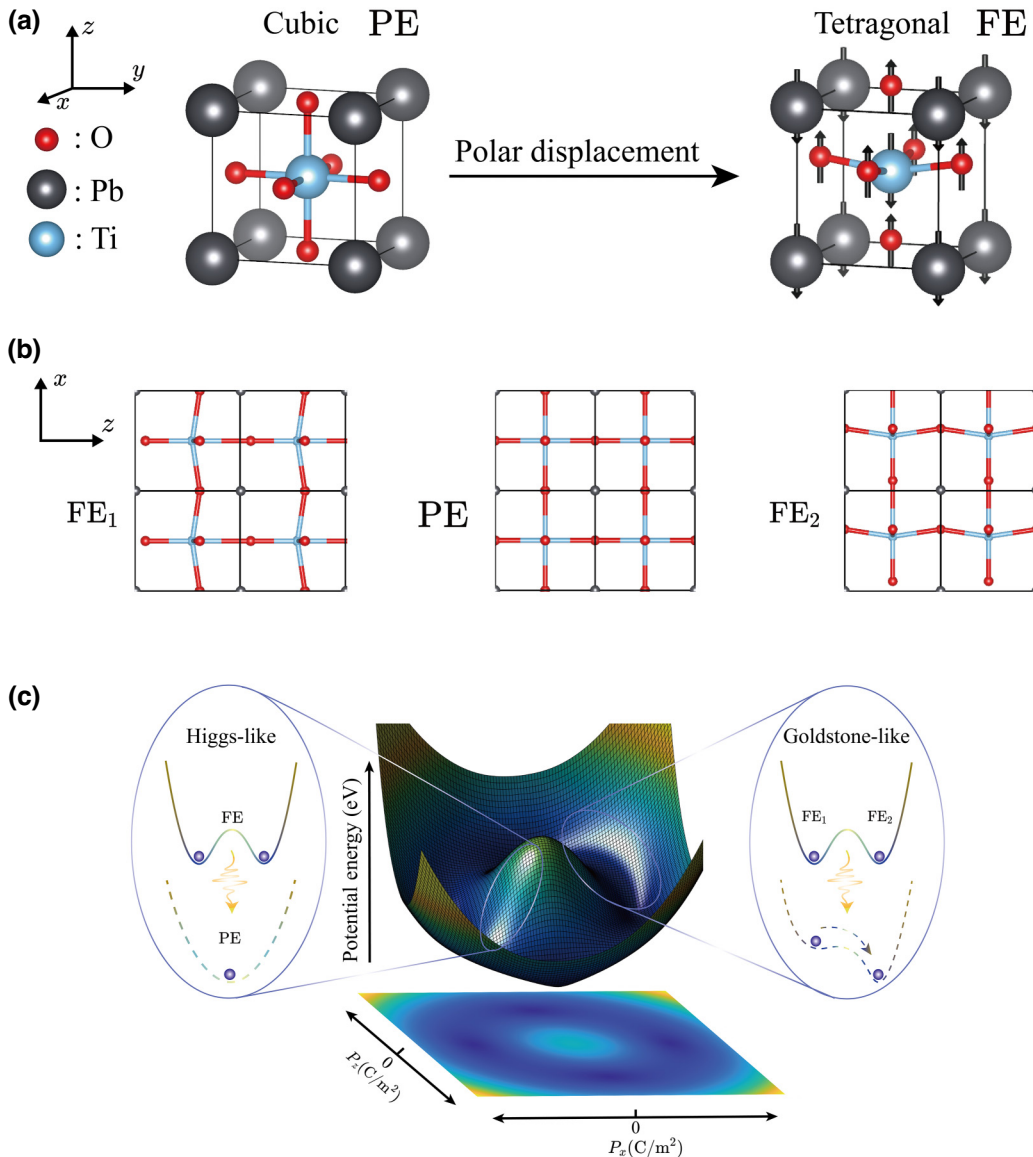


FIG. 1. Schematic illustration of geometric phase transition in  $\text{PbTiO}_3$ . (a) Crystal structures of the cubic paraelectric and tetragonal ferroelectric unit cells. The polar displacement is along the  $z$  axis. (b) The atomic structures of  $\text{PbTiO}_3$  in  $\text{FE}_1$ ,  $\text{PE}$ , and  $\text{FE}_2$  states. (c) Schematic plot of the lattice potential energy surface (PES) with respect to polarizations  $P_x$  and  $P_z$ .

under the depolarization field, leaving the VBM only at  $X$  and  $Y$ . As for the lowest conduction band, one observes almost flat band dispersions along the  $\Gamma$ - $X$  (or  $\Gamma$ - $Y$ ,  $\Gamma$ - $Z$ ) path in the PE phase, which survives only along the  $\Gamma$ - $Z$  in the  $\text{FE}_1$  phase.

The phonon dispersions for both PE and FE phases are plotted in Figs. 2(b) and 2(c). One sees that for the PE structure, the standard second-harmonic vibration results in imaginary modes (dashed curves) in the most part of the first BZ. In order to correct this and include thermal effects, we perform self-consistent phonon calculations. One clearly observes that the imaginary branches are totally suppressed by including the fourth-order anharmonic

coupling effects. Even at 0 K, it is evident that all vibration frequencies become real, showing significant renormalization effects from anharmonic corrections. As the temperature increases, the frequency on each branch enhances to higher frequency. The zone-center phonon frequencies and their irreducible representation and optical activity of  $\text{PbTiO}_3$  are summarized in Table I. The irreducible representations of the twelve optical branches of PE at  $\Gamma$  can be decomposed as  $\Gamma_{\text{op}}^{\text{PE}}(O_h) = 3T_{1u} \oplus 1T_{2u}$ . As for the FE phase, there are no imaginary branches in the second-harmonic framework. The irreducible representations of optical branches are  $\Gamma_{\text{op}}^{\text{FE}}(C_{4v}) = 3A_1 \oplus 4E \oplus B_1$ . In the vicinity of the  $\Gamma$  point, one observes clear

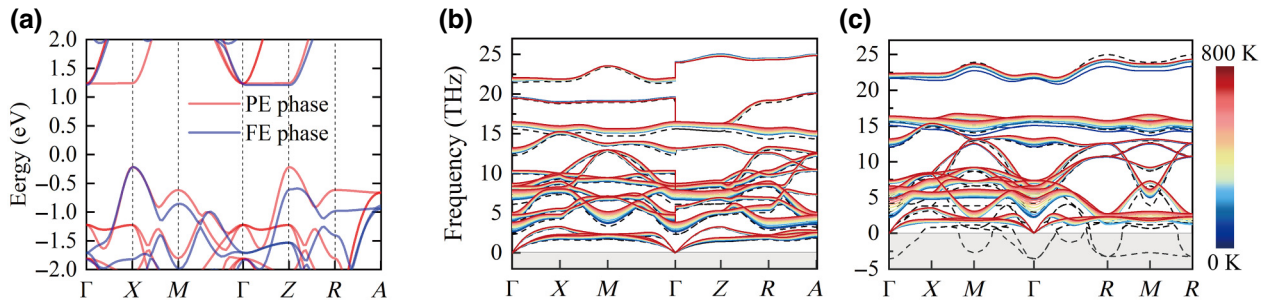


FIG. 2. DFT-calculated fundamental properties of electrons and phonons of  $\text{PbTiO}_3$ . (a) Electronic band dispersion along the high-symmetry  $k$  path, where blue and red curves denote the  $\text{FE}_1$  and PE phase, respectively. The temperature-dependent phonon spectra of the (b)  $\text{FE}_1$  phase and (c) PE phase. The LO-TO splitting effect is included. The gray-shaded areas are the unstable imaginary phonon frequency regime, which is denoted as negative values. The dashed curves represent the phonon dispersion according to the standard second-harmonic approximation, while the solid curves are the finite-temperature phonon structures obtained from the SCPH method.

frequency splitting between the longitudinal optical (LO) and transverse optical (TO) branches, ensuring the large electric dipole effects [37,38].

## B. Optical responses of $\text{PbTiO}_3$ at the THz regime

Next, we calculate the frequency-dependent optical susceptibility tensor  $\chi$  for these two phases, which are used to estimate the Gibbs free-energy variation under linearly polarized terahertz light (LPTL) irradiation (see below and Refs. [39,40]).

The optical susceptibility originates from two sources, namely, electronic and ionic contributions. The large electronic bandgap ( $>1$  eV) guarantees that the electronic contributed susceptibility almost keeps a constant in the THz regime (usually  $\lesssim 0.4$  eV). In the independent particle approximation, it can be evaluated by [41]

$$\chi_{ii}^{\text{el}}(\omega) = \frac{e^2}{\epsilon_0} \int_{\text{BZ}} \frac{d^3k}{(2\pi)^3} \sum_{c,v} \frac{\langle u_{vk} | \nabla_{ki} | u_{ck} \rangle \langle u_{ck} | \nabla_{ki} | u_{vk} \rangle}{\hbar(\omega_{ck} - \omega_{vk} - \omega - i0^+)}, \quad (1)$$

where  $|u_{nk}\rangle$  and  $\hbar\omega_{nk}$  represent the periodic part of the Bloch wave function and its corresponding eigenenergy

TABLE I. The zone-center phonon frequencies (at room temperature), their corresponding irreducible representation, and the basis functions of  $\text{PbTiO}_3$ .

Phase	Frequency (THz)	Irreducible representation	Basis functions
$\Gamma_{\text{op}}^{\text{PE}}(O_h)$	4.6, 6.5, 16.3	$T_{1u}$	$(x, y, z)$
	7.3	$T_{2u}$	—
$\Gamma_{\text{op}}^{\text{FE}}(C_{4v})$	4.6, 10.1, 19.4	$A_1$	$z, x^2 + y^2, z^2$
	3.2, 7.1, 8.2, 16.2	$E$	$(x, y), (xz, yz)$
	8.4	$B_1$	$x^2 - y^2$

for band  $n$  ( $c$  and  $v$  refer to conduction- and valence-band indices, respectively) at  $\mathbf{k}$ . The integral is performed in the first BZ.  $\epsilon_0$  is the permittivity in vacuum, and  $i = \sqrt{-1}$  is the unit of imaginary number. We apply random phase approximation to include its nonlocal effects. Figure 3 plots the calculated diagonal component  $\chi_{ii}^{\text{el}}(\omega)$ . Our calculations reveal that the susceptibility constant for PE is isotropic, namely,  $\chi^{\text{el}}(\text{PE}) = 7.5$ . The electric polarization in the FE phase gives anisotropic results, namely,  $\chi_{\parallel}^{\text{el}}(\text{FE}) = 5.9$  (parallel to electric polarization) and  $\chi_{\perp}^{\text{el}}(\text{FE}) = 6.6$  (normal to electric polarization).

The ionic contribution to optical susceptibility is calculated according to [37]

$$\chi_{ij}^{\text{ion}}(\omega) = \frac{1}{V} \sum_m \frac{\mathcal{Z}_{m,i}^* \mathcal{Z}_{m,j}^*}{\omega_m^2 - (\omega + (i/\tau^{\text{ion}}))^2}, \quad (2)$$

where  $\mathcal{Z}_{m,i}^* = \sum_{\kappa,i'} z_{\kappa,ii'}^* u_{m,\kappa,i'}$  ( $z_{\kappa,ii'}$  is Born effective charge component of ion  $\kappa$  and  $u_{m,\kappa,i'}$  is displacement mode [42,43]) and  $\omega_m$  are the Born effective charge component and eigenfrequency of vibration mode  $m$ , respectively.

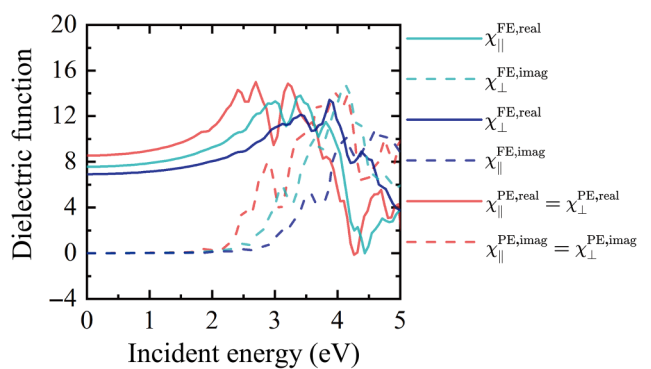


FIG. 3. Real (solid curve) and imaginary (dashed curve) parts of the electronic susceptibility components of PE and  $\text{FE}_1$  phase in the  $\text{PbTiO}_3$ .

The results of Born effective charge of  $\text{PbTiO}_3$  are listed in Table S1 within the Supplemental Material [42].  $V$  is the total volume of the unit cell, and  $\tau^{\text{ion}}$  (taken to be 0.12 THz) represents the ionic vibration lifetime. Note that even though such a lifetime depends on phonon band index and momentum, we follow the conventional treatment to choose a universal value. It does not affect the real part of susceptibility away from the resonant frequency, which is the focus of the current study. We plot the calculated diagonal component  $\chi_{ii}^{\text{ion}}(\omega)$  in Figs. 4(a) and 4(b). The peaks at the imaginary part of susceptibility corresponds to resonant coupling between LPTL and the IR-active modes. According to the Kramers-Kronig relationship, it produces a jump in the real part of susceptibility at the resonant frequency and a nonzero value below such a frequency. For each of the three phases, we observe two dominant peaks at their imaginary-part spectrum. Increasing temperature will shift them toward higher frequencies. Figure 4(c) schematically shows the vibration displacement modes of the first peak in the imaginary part of susceptibility at room temperature. All of them are IR active. At a typical low frequency (e.g., 1 THz), the calculated ionic susceptibility values of the PE phase are 229.5 at room temperature. For the FE phase, the susceptibility at this low frequency  $\omega_0$  is anisotropic, namely,  $\chi_{\parallel}^{\text{ion}}(\text{FE}, \omega_0) = 87.2$  and  $\chi_{\perp}^{\text{ion}}(\text{FE}, \omega_0) = 19.6$  at room temperature. All of the optical susceptibility components (including electronic and ionic contributions) for each phase at 1-THz frequency are listed in Table II. Note that this frequency is away from any IR-active frequencies, hence there is no direct resonant scattering between the LPTL and the ions.

### C. Optomechanics-driven phase transitions in $\text{PbTiO}_3$

The structural phase transition under the off-resonant LPTL irradiation can be conducted by thermodynamic evaluations. The time-dependent alternating electric field  $\vec{\mathcal{E}}(\omega, t) = \vec{E} e^{-i\omega t}$  of LPTL would reduce the Gibbs free energy (GFE) density according to  $dg = -\text{Re} \left\langle \vec{\mathcal{P}}^* \cdot d\vec{\mathcal{E}} \right\rangle$ , where  $\langle \cdot \rangle$  indicates the time average. Note

TABLE II. The ionic and electronic contributions to susceptibility components in  $\text{PbTiO}_3$  and  $\text{BaTiO}_3$  (incident frequency taken to be  $\omega_0 = 1$  THz at room temperature).

Phase		$\chi_{\parallel}^{\text{ion}}$	$\chi_{\perp}^{\text{ion}}$	$\chi_{\parallel}^{\text{el}}$	$\chi_{\perp}^{\text{el}}$
$\text{PbTiO}_3$	PE	229.5	229.5	7.5	7.5
	FE	87.2	19.6	6.6	5.9
$\text{BaTiO}_3$	C	289.4	289.4	5.8	5.8
	T	71.4	32.9	5.7	5.1
	A	61.9	57.5	5.2	5.5
	R	72.8	73.0	5.3	5.3

that the time-dependent electric polarization is  $\vec{\mathcal{P}}(t) = \vec{P}_s + \epsilon_0 \text{Re} \vec{\chi}(\omega) \cdot \vec{\mathcal{E}}(\omega, t)$ , where  $\vec{P}_s$  is spontaneous electric polarization. Since this  $\vec{P}_s$  is generally time independent when the incident electric field strength is below the coercive field (as in the current case), its contribution to GFE would be zero after taking time average. Therefore, the GFE variation under LPTL is

$$G_{\text{LPTL}} \left( \vec{E}, \omega_0 \right) = -\frac{1}{4} \epsilon_0 V \text{Re} [\chi_{ii}^{\text{el}}(\omega_0) + \chi_{ii}^{\text{ion}}(\omega_0)] E_i^2. \quad (3)$$

Here subscript  $i$  indicates the LPTL polarization direction. Note that the integration of  $G_{\text{LPTL}}$  over electric field gives a 1/2 factor, and the time average of the sinusoidal electric field gives another 1/2. Hence, there is a factor of 1/4 in Eq. (3). Accordingly, the optical susceptibility components in different phases determine their total GFE variations under LPTL. If they show large contrast between PE, FE<sub>1</sub>, and FE<sub>2</sub>, LPTL would significantly change the energy profile and one could expect THz light-induced thermodynamic phase transitions.

We include the LPTL contribution into the total GFE [44]

$$G \left( T, \vec{E}, \omega_0 \right) = U - TS + pV + G_{\text{LPTL}} \left( \vec{E}, \omega_0 \right). \quad (4)$$

Here,  $U$  is the total internal energy, and  $S$  is the entropy. We consider only the ion contributed entropy in our discussion, as the electron contributed entropy is significantly small for intrinsic semiconductors with band gap larger than 1 eV. At the pressure-free condition, the third term is safely ignored. Before the LPTL is irradiated, our numerical results yield a FE to PE transition at approximately 720 K, closing to the experimental observations [45]. This also validates the computational approaches with the anharmonic phonon effects.

Without loss of generality, we assume that the light travels along the  $z$  direction, hence the light electric field is polarized in the  $x$ - $y$  plane (we take  $i = x$  or  $y$  here). According to Eq. (4), we now calculate the GFE difference for phase transitions between the FE<sub>1</sub>/FE<sub>2</sub> (Goldstone mode) and FE/PE (Higgs mode), as shown in Fig. 5(a). One sees that before light is introduced (zero electric field), the GFE difference between FE and PE is 48.2 meV per formula unit (f.u.) at room temperature. The two FE phases are energetically degenerate. When we apply a LPTL (at frequency  $\omega_0$ ) with its polarization along  $x$ , the FE<sub>1</sub>/FE<sub>2</sub> degeneracy lifts due to anisotropic optical responses, namely, different  $\chi_{\perp}$  and  $\chi_{\parallel}$ . Hence, we would have a phase transition from FE<sub>2</sub> (smaller  $\chi_{\perp}$ ) to FE<sub>1</sub> (larger  $\chi_{\parallel}$ ). The GFE difference is enhanced to be 14.3 meV/f.u. under the electric field magnitude of 0.5 V/nm, sufficiently large to be distinguished (Goldstone mode). Similarly, as the susceptibility

$\chi$  of PE is much larger than that of the FE. Above a critical electric field of 0.6–0.7 V/nm (depending on the initial structure being  $\text{FE}_1$  or  $\text{FE}_2$ ), the LPTL drives the PE structure to be stable thermodynamically. This implies a FE to PE phase transformation (Higgs mode). These phase transitions do not require any bond breaking and reformation, and involve only collective and coherence atomic displacive motions. Hence, they would occur in a fast kinetics and do not generate significant heat as in the conventional resonant light-absorption mechanism.

Since the 1-THz light is off resonant to excite either an electron-hole pair in electronic band structure or an IR-active mode in the phonon vibration, one may wonder how the light-matter interaction occurs. According to our previous works [39,40], we use a simple expansion on  $\chi$  to propose that it belongs to a second-order nonlinear optical process, which stimulate a Raman-active mode. In this work, we perform an alternating electric field dressed AIMD simulation to illustrate it. We apply the modern theory of polarization to evaluate the time-dependent  $P$  in each step, and multiply it with time-dependent electric field  $\mathcal{E}(\omega_0, t)$ . We then project the ionic vibrational offset into normal coordinates of each phonon calculated by DFPT. Figure 5(b) shows that applying an  $x$ -polarized LPTL onto the  $\text{FE}_1$   $\text{PbTiO}_3$  (under an alternating field with a magnitude of 0.1 V/nm) could induce a nonresonant excitation of phonon mode at 2.3 THz (second-order harmonic calculation). By analyzing the phonon-displacement modes and irreducible representations, we identify that this excited phonon mode corresponds to a Raman-active mode (irreducible representation of  $E$ ) with 3.2 THz frequency in Table I. The different values of frequencies originate from

the anharmonic phonon contribution, which also suggests the useful effect of vibrational anharmonicity. The elicited Raman mode agrees well with its second-order nonlinear optical process nature.

#### D. THz-induced phase transitions in $\text{BaTiO}_3$

In order to show the ubiquity of this optomechanical effect, we take another prototypical perovskite, barium titanate ( $\text{BaTiO}_3$ ), which exhibits more isomeric phases as depicted in Fig. 6. The  $\text{BaTiO}_3$  undergoes displacive structural phase transitions from a high-temperature centrosymmetric phase ( $Pm\bar{3}m$ , denoted as  $C$ ) into tetragonal ( $P4mm$ , denoted as  $T$ ) at 409 K, which breaks inversion symmetry by polar displacements of Ti and O atoms. Below 278 K, it transits into an orthorhombic phase ( $Amm2, A$ ) and then a rhombohedral phase ( $R3m, R$ ) at 183 K [46]. The lattice constants for each phase in  $\text{BaTiO}_3$  are provided in Table S3 within the Supplemental Material [42].

We perform DFT calculations and the self-consistent phonon calculations to evaluate phonon spectra of these four phases, as shown in Fig. 7. Similar as above, we denote two orientational variants of  $T$  phase as  $T_1$  phase (with electric dipole along  $x$ ) and  $T_2$  phase (with electric dipole along  $z$ ). Note that if the standard second-harmonic approximation is applied, only the  $R$  phase shows no imaginary frequencies (dashed curves). In the self-consistent phonon calculation framework, we find all the imaginary phonon branches disappear in all these four phases, even at 0 K. This again suggests the significance of inclusion the high-order anharmonic interactions.

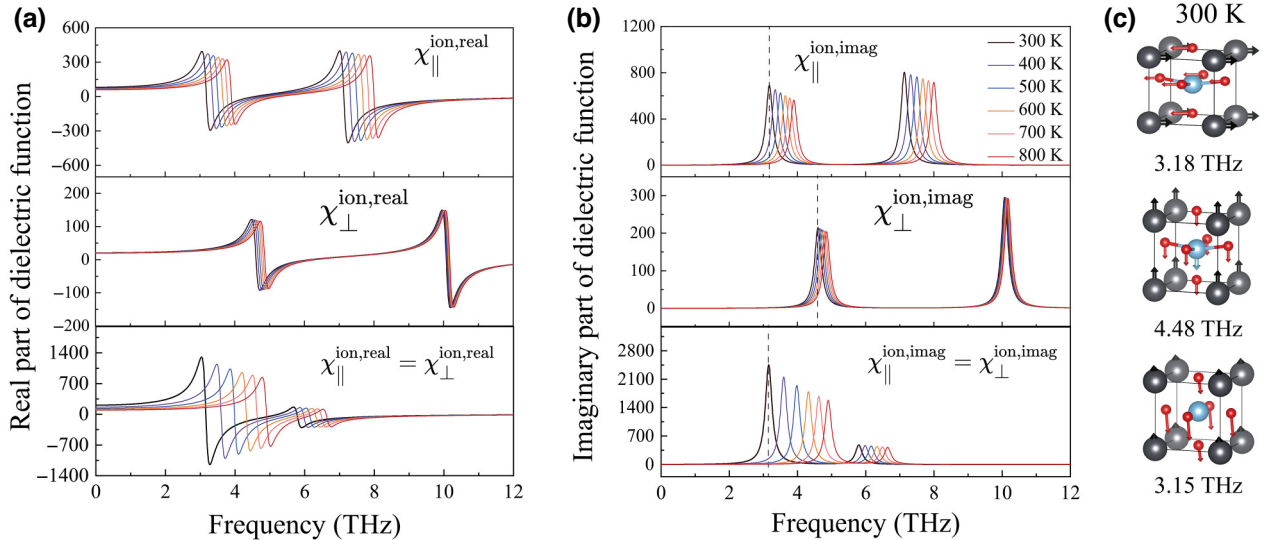


FIG. 4. (a) Real and (b) imaginary parts of the ionic susceptibility components of  $\text{PbTiO}_3$ . The electric dipole for  $\text{FE}_1$  is along  $z$ . The dashed vertical lines in (b) mark the frequency of the first peak in the imaginary part of susceptibility at 300 K. (c) Schematic plot of the ionic displacement modes of the first dominant peak along each direction at room temperature.

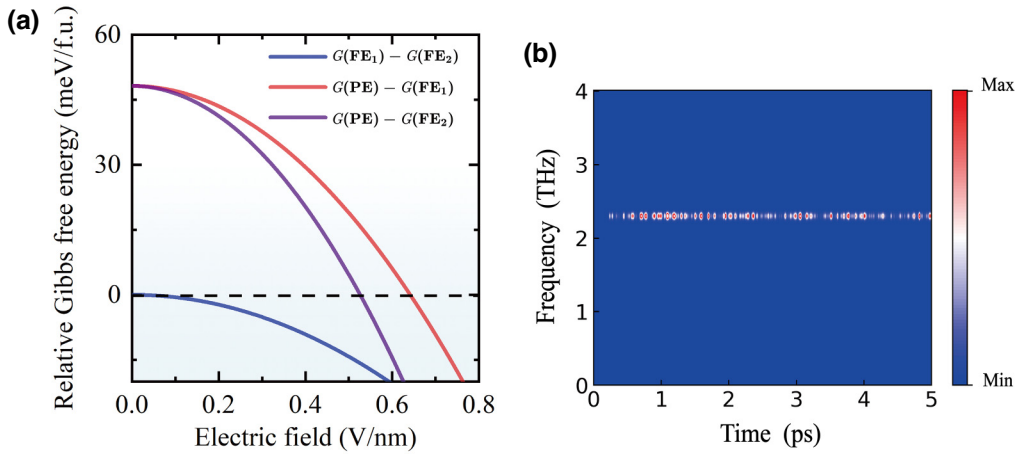


FIG. 5. (a) Relative GFE of  $\text{PbTiO}_3$  as a function of LPTL electric field magnitude at room temperature. (b) Nonresonant phonon response under alternating electric field of FE  $\text{PbTiO}_3$ . Only a Raman-active mode appears here.

We then compute the optical responses of each phase in  $\text{BaTiO}_3$ , which are summarized in Table II. Similar to the previous approach, we compute the electronic and ionic contributions to the dielectric susceptibility of  $\text{BaTiO}_3$  using Eqs. (1) and (2), respectively. Further details can be found within the Supplemental Material [42], which includes the results of the Born effective charge (Table S2 within the Supplemental Material [42]) and the illustration of the diagonal components of  $\chi_{ii}^{\text{el}}(\omega)$  and  $\chi_{ii}^{\text{ion}}(\omega)$

in Figs. S1 and S2 within the Supplemental Material [42], respectively. According to Eq. (4), we estimate the changes in GFE of different phases under 1-THz illumination (at room temperature, with its electric field polarized along  $x$ ), which is depicted in Fig. 8. It suggests that above a critical electric field strength of approximately 0.3 V/nm, the  $T$  phase would transit into the  $C$  phase, which is high symmetric and has vanished spontaneous electric polarization. This thermodynamic result is counterintuitive to

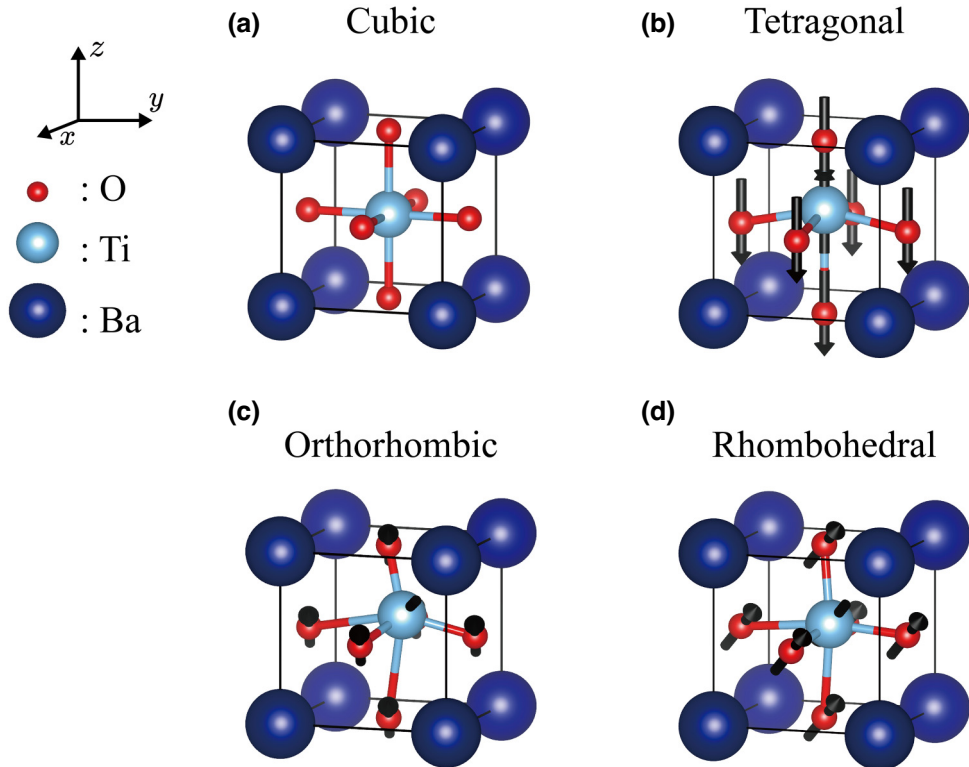


FIG. 6. Geometric structures of  $\text{BaTiO}_3$  in (a) cubic ( $C$ ), (b) tetragonal ( $T$ ), (c) orthorhombic ( $A$ ), and (d) rhombohedral ( $R$ ) phases. The black arrow represents the direction of polarization of the ion (Ti, O) referenced by the  $C$  phase.

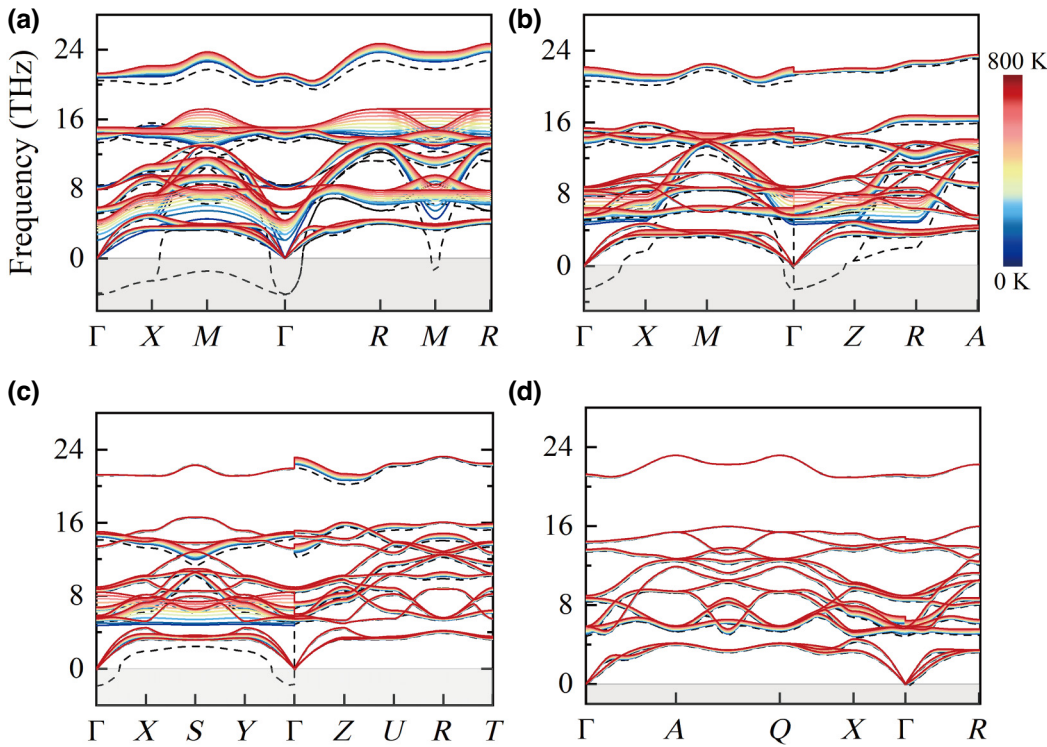


FIG. 7. Temperature-dependent phonon spectra of BaTiO<sub>3</sub> in the (a) C, (b)  $T_1$ , (c) A, and (d) R phase. The dashed curves represent the phonon dispersion according to the second-harmonic approximation, while the solid curves are from the SCPh scheme.

the general physical picture that adding an electric field induces dipole moment (as in the conventional  $E - P$  hysteresis). The underlining reason is that our optomechanical approach contains second-order nonlinear optical response, while the  $E - P$  hysteresis is only the first-order response. In addition, one notes that the C phase usually emerges under high temperature, but here we show that it could appear at room temperature under THz irradiation, being a hidden phase.

#### IV. DISCUSSION

In our study, we have included the LO-TO splitting that naturally occurs in polar materials. It is worth noting that such an effect usually elevates the frequency of the LO mode at the long wavelength limit, while the TO frequency remains almost unchanged [47]. The ion contributed dielectric function is determined by the TO mode near  $\Gamma$  [48], which couples with light electric field. Therefore, the frequency of TO phonons plays a dominant role in the ionic response functions. It can then be inferred that the impact of LO-TO splitting effect is relatively weak in our current study.

During the phase transition and/or a chemical reaction, the energy barrier dominantly controls its kinetics. Unfortunately, it is not straightforward to directly estimate the energy barrier under THz irradiation. This is because the

ill definition of ion vibration contributed dielectric function along the reaction path, where the normalized force is nonzero. Hence, we can only roughly estimate the upper bound of the GFE barrier by the energy difference before light is applied. For the Goldstone mode, we know that there is a small barrier (without light) that separates the two

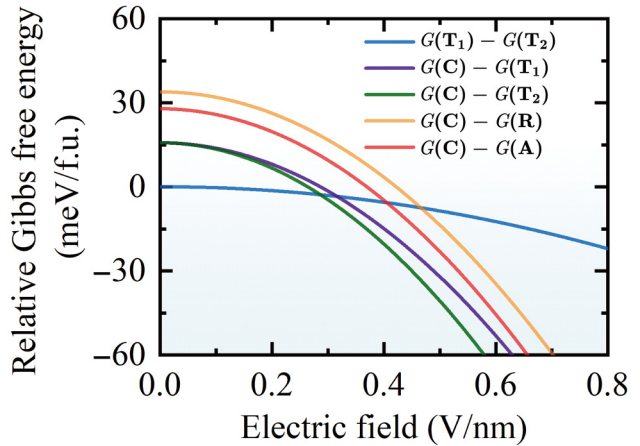


FIG. 8. Relative GFE of BaTiO<sub>3</sub> as a function of the LPTL electric field magnitude under room temperature. The symbols  $T_1$  ( $T_2$ ), C, R, and A denote tetrahedral, cubic, rhombohedral, and orthorhombic phases, respectively. Here  $T_1$  and  $T_2$  refer to that the electric polar direction is parallel and perpendicular to the light electric field direction, respectively.

FE states. Under THz, since the GFE degeneracy of the two FE states is lifted, it is expected that the energy barrier will be reduced. As for the Higgs mode, the FE to PE transformation does not encounter a barrier (without light), as the PE locates at the peak of the energy landscape. Hence, under THz, since the GFE difference between the PE and FE is reduced, we roughly expect that the barrier should be smaller than the total energy difference between the PE and FE. These indicate a reduced barrier as THz intensity is increased, which may facilitate the phase transition under a fast kinetics. We note that this calls subsequent experimental verifications.

One may also wonder whether this optomechanical approach can be used under circularly polarized light (CPL) illumination. Since the CPL carries one imaginary part (a 90° phase difference) in its electric field component, its impact will be related to the imaginary part of the off-diagonal elements in the dielectric tensor [49]. For the perovskites studied in the current work, the high-crystalline symmetry and the time-reversal symmetry guarantees that all the nondiagonal dielectric function elements are zero. This is also verified by our DFT calculations. Nonetheless, in magnetic materials one may use CPL illumination to change their GFE landscape.

Here, we mainly focus on the real part of the dielectric function, as the imaginary part is zero. We have shown that this off-resonant light scattering corresponds to the second-order nonlinear Raman stimulation. We note that it is distinct from previously proposed mechanisms [25, 50, 51], where the THz light resonantly excites infrared-active modes. In such cases, the light-absorption process corresponds to the finite imaginary part of the dielectric function. The infrared-active mode then simulates Raman-active modes via three-phonon or four-phonon interactions, and ultimately drives geometric phase transition. Our optomechanical approach, in contrast, does not require this direct light absorption, which may largely reduce thermal generation.

## V. CONCLUSION

In conclusion, we demonstrate that intermediate THz could drive phase transitions in perovskite oxides such as  $\text{PbTiO}_3$  and  $\text{BaTiO}_3$ , controlling the emergence of ferroelectric polarization and its direction. We show that the anharmonic ionic interactions strongly affect the phonon spectrum and optical susceptibility, which significantly varies as a function of temperature. Using the electric field dressed AIMD simulations, we explicitly show that the off-resonant THz irradiation would evoke the Raman phonon vibration (while it does not need to resonantly excite the IR-active modes). The orientational variant transition provides a theoretical explanation for the recent experimental observations [12]. These optomechanics-induced phase transitions could be easily generalized to other perovskite

systems and ferroelectric materials, serving as an applicable platform for information storage and in-memory computing devices.

## ACKNOWLEDGMENTS

The authors thank Dr Yongliang Shi, Tingwei Li, and Penghu Du for valuable discussions on the simulation procedure, and acknowledge Chuanwei Fan for the computational technical support. This work was supported by National Natural Science Foundation of China (NSFC) under Grants No. 21903063 and No. 11974270. The calculations are performed on the HPC platform of Xi'an Jiaotong University.

- [1] O. Auciello, J. F. Scott, and R. Ramesh, The physics of ferroelectric memories, *Phys. Today* **51**, 22 (1998).
- [2] K. T. Butler, J. M. Frost, and A. Walsh, Ferroelectric materials for solar energy conversion: photoferroics revisited, *Energy Environ. Sci.* **8**, 838 (2015).
- [3] M. Wu, 100 years of ferroelectricity, *Nat. Rev. Phys.* **3**, 726 (2021).
- [4] K. H. Ahn, T. Lookman, and A. R. Bishop, Strain-induced metal-insulator phase coexistence in perovskite manganites, *Nature* **428**, 401 (2004).
- [5] K. J. Choi, M. Biegalski, Y. L. Li, A. Sharan, J. Schubert, R. Uecker, P. Reiche, Y. B. Chen, X. Q. Pan, V. Gopalan, *et al.*, Enhancement of ferroelectricity in strained  $\text{BaTiO}_3$  thin films, *Science* **306**, 1005 (2004).
- [6] Y. Wang, C. Guo, M. Chen, Y. Liang, H. Han, H. Chen, Y. Lin, D. Yi, H. Huang, C.-W. Nan, *et al.*, Mechanically driven reversible polarization switching in imprinted  $\text{BiFeO}_3$  thin films, *Adv. Funct. Mater.* **2213787** (2023).
- [7] W. Han, J. Zhu, S.-j. Zhang, H. Zhang, X.-h. Wang, Q. Wang, C. Gao, and C. Jin, Phase transitions in nanoparticles of  $\text{BaTiO}_3$  as functions of temperature and pressure, *J. Appl. Phys.* **113**, 193513 (2013).
- [8] H. Moriwake, A. Konishi, T. Ogawa, C. A. J. Fisher, A. Kuwabara, K. Shitara, and D. Fu, Polarization fluctuations in the perovskite-structured ferroelectric  $\text{AgNbO}_3$ , *Phys. Rev. B* **97**, 224104 (2018).
- [9] T. F. Nova, A. S. Disa, M. Fechner, and A. Cavalleri, Metastable ferroelectricity in optically strained  $\text{SrTiO}_3$ , *Science* **364**, 1075 (2019).
- [10] F. Chen, Y. Zhu, S. Liu, Y. Qi, H. Y. Hwang, N. C. Brandt, J. Lu, F. Quirin, H. Enquist, P. Zalden, *et al.*, Ultrafast terahertz-field-driven ionic response in ferroelectric  $\text{BaTiO}_3$ , *Phys. Rev. B* **94**, 180104 (2016).
- [11] X. Li, T. Qiu, J. Zhang, E. Baldini, J. Lu, A. M. Rappe, and K. A. Nelson, Terahertz field-induced ferroelectricity in quantum paraelectric  $\text{SrTiO}_3$ , *Science* **364**, 1079 (2019).
- [12] F. Rubio-Marcos, D. A. Ochoa, A. Del Campo, M. A. García, G. R. Castro, J. F. Fernández, and J. E. García, Reversible optical control of macroscopic polarization in ferroelectrics, *Nat. Photonics* **12**, 29 (2018).

- [13] C. Paillard, E. Torun, L. Wirtz, J. Íñiguez, and L. Bellaïche, Photoinduced Phase Transitions in Ferroelectrics, *Phys. Rev. Lett.* **123**, 087601 (2019).
- [14] T. Kampfrath, K. Tanaka, and K. A. Nelson, Resonant and nonresonant control over matter and light by intense terahertz transients, *Nat. Photonics* **7**, 680 (2013).
- [15] C. A. Schmuttenmaer, Exploring dynamics in the far-infrared with terahertz spectroscopy, *Chem. Rev.* **104**, 1759 (2004).
- [16] A. Bera, S. Bera, S. Kalimuddin, S. Gayen, M. Kundu, B. Das, and M. Mondal, Review of recent progress on THz spectroscopy of quantum materials: superconductors, magnetic and topological materials, *Eur. Phys. J.: Spec. Top.* **230**, 4113 (2021).
- [17] T. Dong, S. Li, M. Manjappa, P. Yang, J. Zhou, D. Kong, B. Quan, X. Chen, C. Ouyang, F. Dai, *et al.*, Nonlinear THz-nano metasurfaces, *Adv. Funct. Mater.* **31**, 2100463 (2021).
- [18] J. Bouchard, S. L. Eichmann, H. Ow, M. Poitzsch, and D. T. Petkie, Terahertz imaging for non-destructive porosity measurements of carbonate rocks, *Sci. Rep.* **12**, 18018 (2022).
- [19] Q. Wang, S. Hameed, L. Xie, and Y. Ying, Non-destructive quality control detection of endogenous contaminations in walnuts using terahertz spectroscopic imaging, *J. Food Meas. Charact.* **14**, 2453 (2020).
- [20] G. Tzydynzhapov, P. Gusikhin, V. Muravev, A. Dremin, Y. Nefyodov, and I. Kukushkin, New real-time sub-terahertz security body scanner, *J. Infrared, Millimeter, Terahertz Waves* **41**, 632 (2020).
- [21] Y. Yang, Y. Yamagami, X. Yu, P. Pitchappa, J. Webber, B. Zhang, M. Fujita, T. Nagatsuma, and R. Singh, Terahertz topological photonics for on-chip communication, *Nat. Photonics* **14**, 446 (2020).
- [22] K. Sengupta, T. Nagatsuma, and D. M. Mittleman, Terahertz integrated electronic and hybrid electronic–photonic systems, *Nat. Electron.* **1**, 622 (2018).
- [23] Y. Chen, W. Ma, C. Tan, M. Luo, W. Zhou, N. Yao, H. Wang, L. Zhang, T. Xu, T. Tong, *et al.*, Broadband Bi<sub>2</sub>O<sub>2</sub>Se photodetectors from infrared to terahertz, *Adv. Funct. Mater.* **31**, 2009554 (2021).
- [24] A. Subedi, Proposal for ultrafast switching of ferroelectrics using midinfrared pulses, *Phys. Rev. B* **92**, 214303 (2015).
- [25] M. Kozina, M. Fechner, P. Marsik, T. van Driel, J. M. Glowacka, C. Bernhard, M. Radovic, D. Zhu, S. Bonetti, U. Staub, *et al.*, Terahertz-driven phonon upconversion in SrTiO<sub>3</sub>, *Nat. Phys.* **15**, 387 (2019).
- [26] R. Mankowsky, A. von Hoegen, M. Forst, and A. Cavalleri, Ultrafast Reversal of the Ferroelectric Polarization, *Phys. Rev. Lett.* **118**, 197601 (2017).
- [27] G. Kresse and J. Furthmüller, Efficient iterative schemes for ab initio total-energy calculations using a plane-wave basis set, *Phys. Rev. B* **54**, 11169 (1996).
- [28] J. P. Perdew, A. Ruzsinszky, G. I. Csonka, O. A. Vydrov, G. E. Scuseria, L. A. Constantin, X. Zhou, and K. Burke, Restoring the Density-Gradient Expansion for Exchange in Solids and Surfaces, *Phys. Rev. Lett.* **100**, 136406 (2008).
- [29] P. E. Blöchl, Projector augmented-wave method, *Phys. Rev. B* **50**, 17953 (1994).
- [30] G. Kresse and D. Joubert, From ultrasoft pseudopotentials to the projector augmented-wave method, *Phys. Rev. B* **59**, 1758 (1999).
- [31] H. J. Monkhorst and J. D. Pack, Special points for Brillouin-zone integrations, *Phys. Rev. B* **13**, 5188 (1976).
- [32] T. Tadano and S. Tsuneyuki, Self-consistent phonon calculations of lattice dynamical properties in cubic SrTiO<sub>3</sub> with first-principles anharmonic force constants, *Phys. Rev. B* **92**, 054301 (2015).
- [33] F. Zhou, W. Nielson, Y. Xia, and V. Ozoliņš, Lattice Anharmonicity and Thermal Conductivity from Compressive Sensing of First-Principles Calculations, *Phys. Rev. Lett.* **113**, 185501 (2014).
- [34] R. Iftimie, P. Minary, and M. E. Tuckerman, Ab initio molecular dynamics: Concepts, recent developments, and future trends, *Proc. Natl. Acad. Sci. U. S. A.* **102**, 6654 (2005).
- [35] V. Zelezny, D. Chvostova, D. Simek, F. Maca, J. Masek, N. Setter, and Y. Hong Huang, The variation of PbTiO<sub>3</sub> bandgap at ferroelectric phase transition, *J. Phys.: Condens. Matter* **28**, 025501 (2016).
- [36] J. Léonard, A. Morales, P. Zupancic, T. Donner, and T. Esslinger, Monitoring and manipulating Higgs and Goldstone modes in a supersolid quantum gas, *Science* **358**, 1415 (2017).
- [37] X. Gonze and C. Lee, Dynamical matrices, Born effective charges, dielectric permittivity tensors, and interatomic force constants from density-functional perturbation theory, *Phys. Rev. B* **55**, 10355 (1997).
- [38] X. Gonze, J. C. Charlier, D. C. Allan, and M. P. Teter, Interatomic force constants from first principles: The case of  $\alpha$ -quartz, *Phys. Rev. B* **50**, 13035 (1994).
- [39] J. Zhou, H. Xu, Y. Shi, and J. Li, Terahertz driven reversible topological phase transition of monolayer transition metal dichalcogenides, *Adv. Sci. (Weinh.)* **8**, e2003832 (2021).
- [40] J. Zhou and S. Zhang, Terahertz optics-driven phase transition in two-dimensional multiferroics, *npj 2D Mater. Appl.* **5**, 16 (2021).
- [41] M. Gajdoš, K. Hummer, G. Kresse, J. Furthmüller, and F. Bechstedt, Linear optical properties in the projector-augmented wave methodology, *Phys. Rev. B* **73**, 045112 (2006).
- [42] See Supplemental Material at <http://link.aps.org/supplemental/10.1103/PhysRevApplied.20.024020> for the calculated Born effective charges of PbTiO<sub>3</sub> and BaTiO<sub>3</sub>, the structural parameters of BaTiO<sub>3</sub>, and the diagonal components of the electronic and ionic dielectric susceptibility for each phase in BaTiO<sub>3</sub>, which contains Refs. [42,43].
- [43] R. Resta, Theory of the electric polarization in crystals, *Ferroelectrics* **136**, 51 (1992).
- [44] J. Zhou, S. Zhang, and J. Li, Normal-to-topological insulator martensitic phase transition in group-IV monochalcogenides driven by light, *NPG Asia Mater.* **12**, 2 (2020).
- [45] N. Sicron, B. Ravel, Y. Yacoby, E. A. Stern, F. Dogan, and J. J. Rehr, The ferroelectric phase transition in PbTiO<sub>3</sub> from a local perspective, *Physica B* **208-209**, 319 (1995).
- [46] Q. Zhang, T. Cagin, and W. A. Goddard, The ferroelectric and cubic phases in BaTiO<sub>3</sub> ferroelectrics are also anti-ferroelectric, *Proc. Natl. Acad. Sci. U. S. A.* **103**, 14695 (2006).

- [47] M. Born, K. Huang, and M. Lax, Dynamical theory of crystal lattices, [Am. J. Phys. 23, 474 \(1955\)](#).
- [48] K. Miyata and X. Y. Zhu, Ferroelectric large polarons, [Nat. Mater. 17, 379 \(2018\)](#).
- [49] J. H. Cai, W. Yang, T. J. Zhou, G. Gu, and Y. W. Du, Magneto-optical Kerr effect and optical properties of amorphous  $\text{Co}_{1-x}\text{Si}_x$  ( $0.59 \leq x \leq 0.77$ ) alloy films, [Appl. Phys. Lett. 74, 85 \(1999\)](#).
- [50] A. S. Disa, T. F. Nova, and A. Cavalleri, Engineering crystal structures with light, [Nat. Phys. 17, 1087 \(2021\)](#).
- [51] J. R. Hortensius, D. Afanasiev, A. Sasani, E. Bousquet, and A. D. Caviglia, Ultrafast strain engineering and coherent structural dynamics from resonantly driven optical phonons in  $\text{LaAlO}_3$ , [npj Quantum Mater. 5, 95 \(2020\)](#).